Carbon Sponge-Type Nanostructures Based on Coaxial Nitrogen-Doped Multiwalled Carbon Nanotubes Grown by CVD using Benzylamine as Precursor

Emilio Muñoz-Sandoval, Alejandro J. Cortes-López, Beatriz Flores-Gómez, Juan L. Fajardo-Díaz, Roque Sánchez-Salas, Florentino López-Urías*

Advanced Materials Department, IPICYT, Camino a presa San José 2055, Lomas 4a sección, San Luis Potosí 78216, México.

Abstract

Carbon sponges-type nanostructures (CSTN) based on coaxial nitrogen-doped multiwalled carbon nanotubes (CA-MWCNTs) were synthesized using the aerosol assisted chemical vapor deposition method involving the decomposition of a mixture of ferrocene, benzylamine, thiophene, and ethanol at 1020 °C under a flow of H_2/Ar. Sample morphology and composition profiles were analyzed by scanning electron microscopy (SEM), transmission electron microscopy (TEM), X-ray diffraction (XRD), X-ray photoelectron spectroscopy (XPS), Raman spectroscopy, and thermogravimetric analysis (TGA). SEM and TEM characterizations demonstrated that the CA-MWCNTs consisted of a core MWCNT surrounded by graphite materials with low crystallinity which was confirmed by XRD and Raman spectroscopy. Depending where the CSTN were collected along the reactor, three types of core MWCNTs morphologies were found: (1) N-doped MWCNTs with a bamboo shape and zigzagged growth, (2) straight MWCNTs, and (3) wavy MWCNTs. The carbon CSTN showed to be highly hydrophobic with outstanding oil absorption properties. XPS characterizations suggest the presence of water-fearing chemical groups such as pyrans, furans, epoxies, carboxylic acid (CH_3COOH, ethanoic acid), and ethoxy groups (CH_3CH_2O-) anchored on the surface of the CA-MWCNTs. The mechanism in which the three types of MWCNTs are formed, the nature of the shell disordered graphite materials, and the hydrophobicity of the carbon sponges-type are thoroughly discussed.

Keywords: Carbon, sponges, nanotubes, nitrogen, synthesis, characterizations

To whom correspondence should be addressed: flo@ipicyt.edu.mx
Corresponding author: Tel/Fax: +1 4448342000 (ext. 7238)/+1 4448342010

1- Introduction

Sponges based on carbon nanotube (CNT) networks have attracted attention due to their intrinsic physical-chemical properties [1]. Among the most important properties of the sponges are the hydrophobic and oleophilic properties which could be exploited on environmental remediation in oil spills [2]. Another property is the high surface areas of the carbon sponges that could serve to capture undesirable metals or chemical species in the environment [3]. Furthermore, carbon sponges could be used in the fabrication of supercapacitor, forever-rechargeable battery [4]. Mechanical properties of the carbon sponges are also outstanding; when they are deformed, these recuperate their original form, making them potentially important in the fabrication of artificial muscles [5]. The three dimensional networks in the carbon sponges can serve as scaffolding or a template to grow biological systems such as cell growth and artificial bone production [6]. The production of carbon sponges or carbon nanotube ramifications can be performed using different techniques such as the chemical vapor deposition (CVD) method using a one-step synthesis strategy [7-11], secondary growth CVD method on templates [12-14], and electron beam irradiation at high temperatures [15-17]. Using ferrocene and toluene as precursors in a typical CVD experiment will grow well aligned and straight multiwalled carbon nanotubes (MWCNT) [18].

During the experiment, the idea of introducing foreign atoms into the lattices of the MWCNTs emerged, atoms such as nitrogen [19], boron [20], phosphorous [21], oxygen [22], sulfur [23-30], among others, have been introduced to the graphitic layers of carbon nanotubes. Each atom has an effect on the morphology of the carbon nanotubes, but sulfur and chlorine have played a crucial role in the formation of carbon sponges because sulfur or chlorine produces changes in the grown direction of MWCNTs [7,29]. Carbon sponges made their debut in 2010. Gui et al. [7] reported the synthesis of highly hydrophobic and super-oleophilic carbon sponges using a single-step CVD method involving the decomposition of a mixture of ferrocene ($Fe(C_5H_5)_2$) and 1,2-dichlorobenzene ($C_6H_4Cl_2$) at 860 °C under a flow of H_2/Ar. They found this material can experience large strain deformations and recover to its approximate original shape and high absorption capability (80 to 180 times its own weight). Using the same experimental approach, Hashim et al. [11] synthesized boron-doped carbon sponges with properties similar to those found by Gui et al. [7]. Hashim et al. decomposed a solution consisting of

toluene (C_7H_8), ferrocene, and triethylborane ($C_6H_{15}B$) at 860 °C with an argon flow of 2.5 L/min. Shan et al. [8] reported the use of sulfur in the production of nitrogen-doped multiwalled carbon nanotube (N-MWCNTs) sponges produced by CVD method using combinations of different precursors: **(1)** xylene and sulfur; **(2)** ferrocene and pyridine; **(3)** ferrocene, thiophene and xylene. They found that an increase in the diameter of the CNTs favors an increment in the elastic modulus and a drop in the electrical conductivity of the carbon sponges. Furthermore, Shan et al. claimed that the diameter of the carbon nanotubes can be controlled by changing the concentration of thiophene which was also reported by Wei et al. [31]. It is clear that carbon sponges have proven to be an excellent material for diverse applications; its super hydrophobicity coupled with its amazing oil-absorption capacity make the carbon sponges an excellent candidate for environmental remediation research. Although several efforts have been made to understand the chemical reactivity of the surface of carbon nanostructures through X-ray photoelectron spectroscopy (XPS) characterization and other techniques [32-37], physical and chemical facts of such super hydrophobicity are not entirely clear. Recently, new routes have been proposed to fabricate 3D carbon nanomaterials to be used in different applications [38-41]. Highlights research on the use of such carbon nanostructures for use them as scaffolds in implants [42].

In this letter, the synthesis of CSTN using the Aerosol-Assisted Chemical Vapor Deposition (AACVD) method is reported. Ferrocene and thiophene are dissolved in a solution containing benzylamine and ethanol. The samples are characterized by means of SEM, TEM, XRD, XPS, TGA and Raman spectroscopy. In order to quantify the degree of graphitization of the carbon sponges, a deconvolution by the XRD (002) peak was performed. XPS spectrum also was deconvoluted to identify the different types of chemical species, functional groups, carbon materials (sp^2 or sp^3 bonding), nitrogen doping (N-quaternary, N-pyrrolic, N-pyridine), the C1s, N1s, and O1s. Furthermore, density functional calculations in N-doped and pristine bilayer graphene with intercalated H, Fe, and O are performed to elucidate the effect in the interlayer distance. To the best of our knowledge, investigations of carbon sponges using unconventional benzylamine and ethanol solutions in a CVD arrangement at high temperature have not been reported.

2- Methodology

2.1 Experimental details

CSTN were produced by the AACVD technique involving the decomposition of a mixture of ferrocene (1.6 %), benzylamine (48.7 %), thiophene (0.3 %), and ethanol (49.4 %) at 1020 °C under a H_2/Ar carrier flow of 0.8 l/min for 2 hours growth. The grown material was collected from the reaction quartz tube by scraping its inner walls. The samples were classified according to the zone where they were grown. In figure 1a, a schematic representation of the AACVD setup is displayed, the different regions alongside the reactors are labeled by "S". According to the temperature profile along the reactor (see figure SI-1); S3 and S4 have the highest temperatures. Electron microscopy: SEM (Helios Nanolab 600 Dual Beam) and HRTEM (FEI Tecnai F30) were used for morphological characterization of the samples. For SEM, small amounts of as-synthesized material were deposited on carbon tape over aluminum pins. For HRTEM, small amounts of the samples were ultrasonicated in ethanol and deposited over copper holey carbon TEM grids. Synthesized samples were analyzed with a Renishaw microRaman spectrometer with a 633 nm excitation laser wavelength. The nitrogen content in the CSTN were measured by X-ray photoelectron spectroscopy (XPS) using a PHI 5000 VersaProbe II equipment with a monochromatic Al-κα source (1486.7 eV). Thermo-gravimetric analysis were performed using a STA 6000 Perkin-Elmer under the following conditions: Samples were heated in simultaneous thermal analyzer in a temperature range of 50 – 950°C with heating speed of 10°C/min under dynamic flow of oxygen (20 mL/min). X-ray powder diffraction patterns were obtained using a Bruker XD8 ADVANCE. The deconvolution analysis was performed using the software Spectral Data Processor SDP 4.1. For the quantification of superhydrophobicity the angle of contact was measure four times to each sample using a ramé-hart instrument. For absorption measurements, the sample were submerged in the substance and weighted in a balance Mettler Toledo Modelo: XS205 several times. For the oil absorption test a mixed substance of Canoil cooking oil and Pinto color oil was used. Methanol, chloroform, pump oil, diesel, gasoline, vegetable oil, N,N-dimethylformamide, ethylene glycol also were used to test the absorption capacity of CSTN. Samples < 5mg of CSTN material was previously weighed then dropped over the substance and left there over 5 min. The relation between the volume absorbed and the initial volume of the CSTN was calculated. We also obtained BET isotherms were obtained in Quantachrome NOVA 1200e equipment following the next conditions. Samples were degassed by 13 h

keeping a heating temperature of 200 °C then N_2 gas was used as analysis gas to be physisorbed on the carbon nanotubes surface.

2.2 Theoretical details (cuidado con las referencias)

Structural and electronic properties of single layer and double layer graphene were simulated using Density Functional Theory [38]. Spin polarized calculations were performed using the generalized gradient approximation (GGA) [39] with PBE parametrization was selected for the exchange-correlation functional [40] implemented in the SIESTA code [41,42]. The wave functions for the valence electrons were represented by a linear combination of pseudo-atomic numerical orbitals using a Double-ζ basis (DZP), while core electrons were represented by norm-conserving Troullier-Martins pseudopotentials in the Kleyn-man-Bylander non-local form [43,44]. The real-space grid used for charge and potential integration is equivalent to a plane-wave cut-off energy of 150 Ry. The pseudo-potentials (pp's) were constructed from 1, 4, 5, 6, and 8 valence electrons from the H, C, N, O, Fe ions (H:$1s^1$, C:$2s^22p^2$, N:$2s^22p^3$, O:$2s^22p^4$, and Fe:$3d^64s^2$). The single and two layer graphene were simulated with a 5×5 superlattice with 72 and 144 atoms respectively. We have considered 10×10×1 k-points, periodic boundary conditions for two dimensional systems, and an inter-structures distance was kept to a minimum of 30 Å in z-direction to avoid lateral interactions. In the calculations, all atoms contained in the system were relaxed using a conjugated gradient and variable cell methods, the total energy was calculated when the forces were converged to less than 0.04 eV/Å. The binding energy is determined by means of $E_{bind}=E_{syst} - n_N E_N - E_{Fe} - nc E_C$, where E_{syst} is the total energy of the complex system. E_N, E_{Fe}, and E_C are the energies of isolated N, Fe and C atoms respectively. Values of n_N, n_{Fe}, and n_C correspond to the number of N, Fe and C atoms respectively. The formation energy was determined by $E_{form} = E_{syt} - E_{2LG} - n_N \mu_N + n_c \mu_C - \mu_{Fe,O,H}$. E_{2LG} refers to the total energy of pristine bilayer graphene. Here μ_X (X=H, C, N, O, Fe) correspond to the chemical potential. The chemical potential of μ_N, μ_C, and μ_O were determined from N_2, O_2, and

H$_2$ molecules respectively whereas the values of μ_C and μ_{Fe} were calculated from graphene pristine and Fe-bulk-crystal structure respectively. n_N corresponds to the numbers of nitrogen atoms and nc corresponds to the removed or added carbon atoms.

3-Results and discussion

SEM Characterization: Figure 2 displays SEM images for samples synthesized at 1020 °C with an Ar/H$_2$ gas flow of 0.8 l/min. Samples from S1 and S2 were collected at the exit of the tubular furnace. The samples consisted of flakes formed by multilayered carbon materials with a brittle texture on one side and the other seemingly rough (see figure SI-5 in Supplementary Information). For sample S1, the lateral dimensions of flakes are larger than for S2. For S3, the formation CNTs exhibited two types of diameters; CNTs with a diameter of ~300 nm with a wavy tubular structure and CNTs with a diameter of ~50 nm displaying a straight structure. Most of the wavy tubular with diameters of ~500 nm were grown in the S4 zone. It was also found that CSTN in S4 region can be detached from the quartz tube in large pieces (~15 cm long). Similar to the sample S4, sample S5 exhibited 300 nm long CNTs, but the structures were straight and short in length. In the S6 zone, graphitic ribbons and CNTs linings were obtained. In conclusion, the sample profile alongside the tubular furnace axis presents five common morphologies: flakes, straight CNTs, wavy CNTs, graphitic ribbons and CNTs linings.

XRD characterization: To elucidate the crystal structure of carbon materials involved in the different zones, XRD characterizations were performed. Figure 3 displays the XRD patterns of the different collected samples. First, we analyzed the peak related to C(002) plane of the hexagonal graphite structure (see figure 3a). It was observed that the C(002) peak presents a strong dependence with the sample type, for instance, samples S1, S2, S3, and S4 display a symmetrical broad peak, which can be fitted to Gaussian and Voigt curves, conversely samples S5 and S6 exhibit a clear C(002) peak with an asymmetric shape. A deconvolution analysis of the C(002) peaks allowed identification of the degree of graphitization of the samples. In our case, the C(002) peak is fitted using two curves. The first curve (band-γ) is associated with no hexagonal conventional carbon (turbostratic graphite or intercalated material graphite) whereas the second curve (band-π) is related to the graphitization (graphite with the

conventional AB stacking). Table 1 shows a complete analysis of the C(002) peak deconvolution for all the samples. The area under the curves provides information on the quantity of graphite-like materials and the other carbon materials containing at the sample. The interlayer distance d_{002} is derived from Bragg´s law. The deconvolution analysis suggests two important points: (1) samples S1 and S2 exhibit a graphitization of ~62% with an interlayer spacing of ~3.43 Å, the remaining material is made from graphitic-like materials with spacing of layers of ~3.73 Å, indicating a probably presence of intercalated materials in the graphitic layers; (2) samples S3, S4, S5, and S6 exhibit low graphitization, for instance, for sample S4 only, 19 % of graphitization is obtained with an interlayer spacing of ~3.38 Å, the remaining material, unconventional carbon, could have come from a more dominant presence in the sample exhibiting an interlayer spacing of 3.47-3.58 Å, which could probably be associated with the presence of Fe atoms or other chemical species intercalated into the graphitic layers as it will be seen later. XRD had results within the ranges of 30-60 degrees, which are shown in figure 3b, thus proving the presence of catalytic nanoparticles. The corresponding intensity peaks associated to Iron carbide and γ-Fe in bulk phases were indexed. Broad peaks exhibited by the samples S1 and S2 suggest the presence of small catalytic particles. In samples S3, S4, S5, and S6, the XRD plots show defined peaks associated to Fe_3C and γ-Fe. The presence of narrow peaks is clearly observed in S6 sample, this evidence suggests the existence of large sized catalytic particles.

TEM characterization: Figure 4 displays TEM images of the synthesized **S6** samples as representative sample of CSTN. This sample exhibits carbon junctions of approximately 200 nm in diameter can be observed in figure 4a, these types of junctions were particularly observed in the S6 zone. It seems that such structures were formed in two steps, namely: first CNTs were catalyzed by iron-carbide nanoparticles; second, CNTs forming T shapes were coated by layered graphite networks. In figure 4b a close up of the carbon nanotube junction is depicted, notice that the carbon nanotubes form a T-type junction. A high magnetization of the junction shows the layered material (see figure 4c). A large carbon fiber is indicated by the arrow in figure 4d. It was found that CSTN are composed by a complicated structure consisting in inner CNTs with well aligned graphite layers surrounded by a shell of carbon layers with low crystalline structure (see figure 4e). The arrow in figure 4e depicts an iron-base nanoparticle, a close up image of the nanoparticle can be observed in figure 4f where it is easy to see a

shell covering the nanoparticle. Figure 4g shows the typical sponge-type structure with elbows and curly morphologies. Figure 4h demonstrate that the CNT linings are made of graphite layers with low crystal structure. Figure 4i shows iron-base nanoparticles and hollow carbon nanotubes, which are indicated by the black and white squares, respectively, a close up of the images are also shown in figure 4j and 4k respectively. The nanoparticle in figure 4j was identified as Fe_3C phase with an inter-planar spacing of d=0.235 nm between crystallographic planes belonging to the family (1,2,l). In the case of figure 4k it seems that the iron-base nanoparticles was not completely encapsulated and was released in the process of sample preparation. It was also found in S6 zone structures showed in figure 4l. They are carbon graphite ribbons catalyzed by the iron-base nanoparticles. During the formation of these graphite ribbons, they are coated by graphite layers which are subsequently detached. Figure SI-9 are TEM images to exhibit a global view of the S1-S5 samples. Their morphological particularities are described in the footnote. The main building blocks of CSTN are the straight and wavy carbon nanotubes. These structures can present wide and narrow diameters.

Raman characterization: Figure 5 shows the Raman spectrum for the different synthesized samples. The peak G refers to sp^2 hybridization whereas D peak indicates a disorder very probably due to the following scenarios: i) nitrogen doping; ii) functional-groups (ether-, ester-, carboxylic-, carbonyls, hydroxyl-groups) that attached themselves to the carbon fibers; or 3) morphological defects. The vertical lines in figure 5 depict the typical frequency values for the D and G peaks. For instance, the associated G-peak (1597 cm^{-1}) is well centered for sample S6. CSTN that are presented in samples S4 and S5 exhibit a downshift G-peak. It was found that in all samples exhibiting a downshift D-peak (1354 cm^{-1}) indicated disorder in the sample due likely to sp^3-hybrized carbon atoms. A broad peak with very low intensity for the 2D mode around 2700 cm^{-1} was observed (non-shown) more clearly for samples S3, S4, S5, and S6. In general, Raman characterizations reveal the presence of the typical D, G, and 2D peaks of graphitic materials, indicating traces of sp^2 and sp^3 carbon materials. Since the frequency of the G peak is related to tangential C–C bonds in an aromatic environment, the frequency downshifting is likely associated to the foreign atom intercalated between the graphite layers which has modified the C–C bonds.

XPS characterization: Figure 6 displays C1s, N1s, and O1s spectra results derived from high resolution XPS characterization. From spectral-deconvolution of C1s and O1s, the identification and concentration of oxygen functional groups were estimated. The spectrum-deconvolution of N1s provided information on how the nitrogen is embedded into the graphitic layers. The spectral-deconvolution results are shown in tables 2, 3, and 4 for C1s, N1s, and O1s respectively. In figure 6a the C1s spectrum is shown, the vertical lines indicate the different oxygen functional groups and type of carbon materials (sp^2 or sp^3). The presence of sp^2 (~284 eV) and sp^3 (~285 eV) is clearly identified for each sample. In all cases, the samples contain a greater contribution of sp^3 than sp^2 bonding, except in sample S1. It was also observed that the hydroxyl groups (~286 eV) are more notable for samples S4, S5, and S6. Notice that a XPS signal around 289.1 eV is identified, which can be attributed to carboxylic groups (see figure 6a). The C1s spectrum was deconvoluted using Gaussian curves (the most robust peak), proving interesting trends of the concentration of the different types of chemical species. Thus, the integrated area of the different Gaussian curves provides an estimation of the percentage of chemical species contained in the sample (at least in the range of integration). For instance, the integrated area of sample S1 yields 44.8 % and 56.2 % of sp^3 and sp^2 carbon materials respectively. It was found that the sp^2 carbon materials decrease for samples collected close to the furnace inlet; see data for S4, S5, and S6, in table 1. Also, an important increment of oxygen functional groups is obtained for samples S4, 5, and 6 samples (285.49-286.19 eV). It is important to mention that highly hydrophobic CSTN were collected in these samples; larger quantities were found in the S4 and S5 samples. The N1s spectrum is displayed in figure 6b, the type of doping is indicated by the shaded regions. We have also deconvoluted N1s peak to provide information on pyridic N (N surrounded a carbon vacancy), pyrrolic N (N in a pentagonal carbon ring), and quaternary N (N in a hexagonal carbon ring), see table 2. Besides, the area under the Gaussian curves of the deconvoluted N1s peaks provides an estimation of the percentage of quaternary, pyrrolic, and pyridinic N-doping. Sample S1 exhibits mostly nitrogen atoms incorporated in the carbon lattice via quaternary and pyrrolic fashions (see table 2). In the S4 sample, the N-quaternary percentage (29.3 %) is reduced with respect to the S1 sample (46.2 %), but an increment in the N-pyrrolic percentage is obtained (53.1%), also the N-pyridinic percentage increased. The N-quaternary percentage is even more incremented for samples S5 and S6. In general, the N-pyrrolic and quaternary doping is favored for all samples, sample S4 contained high amounts of N-pyrrolic (53.1 %) which corresponds to the wavy

carbon fibers. N-pyridinic doping was the least favored in all samples (see table 2). In order to corroborate the XPS results we performed FTIR characterization in our samples (see figure S-11). According this figure the main contribution correspond to the strong signal of C=C sp^2 bond (1500-1550 cm^{-1}) related with the graphitic material. The aliphatic CH$_2$ and CH$_3$ (2859 cm-1 – 2970 cm^{-1} with its conjugate at 1336 cm^{-1}) also are important. The C=O bond due the ester formation can be found at 1749 cm^{-1}. Although the C-O (ester group) was found only for the S6 sample at 1244 cm^{-1}, it is possible that is present in the other samples.

Figure 6c displays the typical O1s spectrum indicating the presence of different types of oxygen functional groups and contents. The results of the deconvoluted C1s peaks are shown in table 3. The deconvoluted C1s spectrum revealed that sample S1 exhibits oxygen-physically absorbed (~530.69 eV), hydroxyl-groups and carboxylic-groups can also detected at ~532.09 eV and 533.38 eV respectively. For sample S4, hydroxyl-, ether-, and ester- groups can be associated to the 531.55 eV, 532.48 eV, and 533.60 eV respectively. The ethoxy groups (CH$_3$CH$_2$O-) and carboxylic acid (CH$_3$COOH) can attach to the Fe atoms hosted on the surface of the carbon fibers. According the deconvolutions of XPS results exhibited in table 4, these functional groups were also observed in samples S5 and S6. It is important to mention that ether- and ester-groups could be responsible for the hydrophobic behavior of samples S4, S5, and S6. There was an interesting observation that was detected in sample S5; there was a large content of carboxylic groups which are known to be hydrophilic. SEM characterization validates that the increment of the carboxylic acid is due to the carbon fiber morphologies which consists of straight short carbon fibers, therefore the carboxylic-groups could be hosted in the tips of the carbon fibers.

Thermogravimetric Analysis: Figure 7 shows the TGA results for S4 and S5 samples with zigzagged and straight carbon fibers respectively. The TGA of the S4 sample exhibits two important weight losses of ~3.13 wt% at 325.33 °C and ~74.22 wt% at 628.43°C. For the S5 sample there is a weight loss of ~93.42 wt% at 627.76 °C. The drop of weight in sample S4 is likely due to organic C-O-C functional groups which could be attributed to pyrone, chromene, lactone, and lactol. By the deconvolution of the

O1s XPS spectrum (figure 6c), we found that among all samples, the S4 sample exhibits the maximum amount of organic C-O-C groups (the integrated area of the assigned peak yields 38%, see table 4). The existence of these functional groups only can occur at graphitic edges. Therefore TGA results suggest the existence of a defected carbon surface with edged layers.

Density Functional Theory Calculations: we performed first-principles calculations in nitrogen-doped graphene bilayer containing different intercalated species (see figure 8) [46-47]. Hydrogen, oxygen, and iron intercalated graphene bilayer were considered. After geometry optimization, the interlayer spacing was determined for H-intercalated bilayer, an interlayer distance of 3.75 Å was found, which can be related to samples S1 and S2 as XRD characterization revealed (see table 1). For Fe-intercalated bilayer, the optimized interlayer distance yields 3.54 Å, this result can be related to samples S3, S4, S5, and S6 (see table 1). Furthermore, O-intercalated bilayer calculations were performed; the interlayer distance was about 4.41 Å. Our DFT-calculations suggests that different intercalated material can be hosted and the strongest candidates seem to be H and Fe. In order to support this claim, the different values for the binding, formation energies, interlayer distance and magnetic moment for different scenarios of intercalated atoms between carbon layers were calculated and presented in Table S-5. As can be in this table H and Fe atoms present the more favorable schema. A stacking AB was chosen because it is the energetically more stable.

To elucidate on the interaction between the graphitic layers and chemical functional groups, we have calculated two functional groups derived from ethanol with C=O and C-O bonds from carboxylic and ethoxy groups, respectively. CSTN samples exhibit C=O and C-O bonds from our XPS characterizations. These chemical functional groups contain methyl groups in the tail, which are hydrophobic groups (non-polar feature). Structure optimization of these groups on graphene, the chemical groups are not covalently attached, conversely Fe on graphene help to join the functional groups in a covalently fashion (see figure SI-1 in Supplementary Information). The carboxyl acidic, ethoxy groups and other chemical groups could also join to graphitic layers via N-doping and defects (vacancies, edges, no hexagonal carbon rings, etc.). More investigations of the origin of the

hydrophobicity in our sponge-type structures and also on the different reported carbon sponges in the literature are needed.

Hydrophobicity, oil-absorption, and oil-burning test: The hydrophobicity of CSTN samples was quantified by the measure of contact angle [50] checked for two different ways: **(1)** a pristine S4 sample was placed on a glass microscope slides and a droplet of deionized water was dropped on it. The estimated contact angle was around 150° demonstrating that CSTN are superhydrophobic [kennet]. Additionally, a second droplet was placed on the glass for comparison (see figure 9a, see right side); **(2)** sample S4 was sonicated in ethanol for 2 hours and filtered under vacuum using nylon membranes of 200 nm porous size. Figure 9b and 9c shows droplets water on CSTN materials derived from later way. To test the oil absorption properties of CSTN, a mixed oil substance consisting in cooking oil and color oil was sonicated during 30 minutes. The resultant oil was dropped in deionized water contained in a beaker. After 5 minutes, a piece of CSTN was placed on the oil mixture and the evolution was monitored by taking a photograph at 0, 3, 6, 13, 31, and 57 s (see figure 10). The sample was saturated at ca. 57 s. Figure 11 shows typical burning process of oil saturated STS material. CSTN texture and properties was not affected due to the burning process. The oil was totally burned in 3 minutes. CSTN materials are able to absorb 10 times its weight. The results for ethanol, chloroform, pump oil, diesel, gasoline, vegetable oil, N,N-dimethylformamide, ethylene glycol are exhibited in figure 12. The volume before that CSTN were used in absorption experiments was approximately 0.15 cm^3 (see figure 12a) and after of absorption was ~180 cm3 (see figure 12b). This figure also shows how CSTN changes due de absorption process. Before vegetable oil absorption, the volume of CSTN was 0.149 cm3 and after the volume changed to 0.178 cm3. Figure 12c shows a relation between the capacity absorption and the solvent density, where the chloroform and the ethylene glycol are the highest absorbed solvents. Figure 12d elucidates a comparison between the materials reported by Gui et al. [7] and our CSTN material. It is observable than the capacity absorption of the CSTN material (red bar) is competitive with other sponge type materials like nanowire [yuan], hydrophobic polyurethane sponge [peng] or polyester sponge [7]. Table SI-2 shows the quantitative results of absorption capacity of CSTN sample. We consider that CNTS is a competitive material in this regard. Table SI-3 show the absorption capacity

values that have been reported by other researchers. According this table our material show interesting values that makes it in a competitive material.

How the CSTN grow and why they are super hydrophobic? In this section, based on the characterization results shown above, we discussed the possible mechanisms of growth and the super-hydrophobicity of the carbon sponges. The sponges contain mainly zigzagged, straight, and wavy fibers. The zigzagged fibers were obtained from a hot zone in the reactor, the XPS characterization indicated the existence of large amounts of N-pyrrolic which is an indication of bamboo-shaped structures, which was also confirmed by TEM characterization. Carbon fibers with bamboo-like structures favored a zigzagged growth. Regarding straight carbon fibers, it was observed that straight fibers contained multiwalled carbon nanotubes with around 15 nm internal diameters most likely due to the growth of FeS_x surrounding the Fe nanoparticles in the early growth stage (FeS_x−Fe eutectic alloy phase). The wavy fibers contain multiwalled carbon nanotubes with large internal diameters most likely due to the presence of large FeS_x clusters on Fe nanoparticles. The wavy carbon fibers were found in the S6 zone (reactor entrance) where the sulfur concentration was high, whereas straight carbon fibers were found in the S5 zone (inward reactor) where the sulfur concentration was less than that found in the S6 zone. Therefore the diameter of the carbon nanotubes depends on the sulfur concentration in accordance with previous reports [8,31].

Since the hydrophobicity occurs on the surface, it is important to understand how the last or the outermost layer of carbon fibers is formed. In the experiment, several precursors in the atmosphere such as ethanol, thiophene, benzylamine, and ferrocene were whole or moderately decomposed depending on the temperature of decomposition and the turbulent internal activity. Taking into account that the temperature range of decomposition of ferrocene, ethanol, thiophene, and benzylamine is 400-500 °C, 772-807 °C, 800-900 °C, and 952-1325 °C respectively, it is probably that Fe atoms could be hosted on the surface of the carbon fibers. In the integrated area of the deconvoluted C1s peak, the CSTN contain large amounts of sp^3 carbon materials, enhancing up to 52% for the sample S4, which is likely due to the presence of Fe atoms or four coordinated carbon atoms contained in the functional groups. The organic C-O bond is a characteristic of hydrophobic functional groups; carboxylic acids and ethoxy groups, whereas organic C=O bonds are found only in carboxylic acids. We found that the concentration

of carboxylic acids or ethoxy groups is strongly dependent on the nature of the sample. For example, for the S4 sample, there were ~23% of C-O bonds and ~38% of C=O bonds, indicating that the concentration of carboxylic acids is larger than that of ethoxy groups. Although hydroxyl groups (C-OH) and carbonyl groups (C=O) are usually hydrophilic, this fact is valid when these groups are directly attached to carbon materials, for example, graphene oxide. Our XPS characterizations provide evidence on the presence of C-O and C=O bonds, but probably associated to epoxy, ethoxy and ester groups, which are normally hydrophobic and in most cases are not hydroxyl. Since our CSTN the samples are highly hydrophobic (see Figure SI-7) it is plausible that the second scenario is happening In order to clarify the previous argumentation we performed calculations of ester and ethoxy groups anchored to the surface of CSTN via a Fe atom (see figure 14a) and via nitrogen or vacancy sites (see figure 14b). According this calculation these scenarios are energetically stables and promote that the distance between carbon layers increased as X-ray and TEM results showed. Based on this theoretical calculations in combination of the obtained C1s XPS spectrum, we could suggest that Fe atoms or carbon fiber defects could serve as anchoring sites for ethoxy groups or carboxylic acids is one of the possible scenarios for the experimental observation of superhydrophobicity in our CSTN materials.

We synthesized CSTN at 960 °C with the other parameters intact. The morphologies obtained in different places of the reactor are shown in figure SI-2 and figure SI-3 (see Supplementary Information). From S1-S3 regions the samples exhibit no or few formation of carbon nanotubes, several graphitic flakes can be observed see figure SI-(a-c). Figure SI-2d depicts the morphologies of carbon nanostructure synthesized in region S4, straight nanotubes of ~80 nm in diameter with several nanoparticles on their surface, also large diameter of ~400 nm can be also observed. In S5 sample graphitic nanoribbons and straight carbon nanotubes were observed, se figure SI-2e. Figure SI-2f depicts the carbon structures obtained in sample S6, the structures consist of graphitic nanoribbons with nanoparticles (up to 200 nm in diameter) in the tip, notice also that several nanoparticles with of few nanometers ~10 nm in diameter are attached on the surface of nanoribbons. TEM images shows clearly the graphitic nanoribbons with nanoparticles inside or on their surface, see figure SI-3. In order to elucidate on the different materials synthesized, we performed. XRD characterizations, the patterns changed according the sample type (see figure SI-4 and table SI-1 in Supplementary Information).

When we compared with the experiment at 1020 °C, the (002) graphite is narrower and more broad peaks in the range of 40-46 degrees suggest well-ordered graphitic materials and nanoparticles in the samples synthesized at 960 °C. Although some zones present comparable structures than the 1020 °C case, the high temperature is fundamental for the formation of CSTN architecture.

5-Conclusions

Synthesis and characterization of nitrogen-doped CSTN were performed by means the CVD method. SEM and TEM characterizations revealed that different carbon morphologies are synthesized alongside the reactor. Flakes formed by well-stacked graphitic layer were formed at the exit of the reactor and carbon sponges were found predominantly in the center of the reactor. An exhaustive deconvolution analysis of graphite peak (002) of the samples revealed the existence of different inter-layers graphitic materials, suggesting the presence of atoms hosted inside the layers. Using DFT calculations, we demonstrated that the increment of the interlayer distance of carbon flakes could be due to the H intercalation, whereas the carbon fibers might be due to the Fe intercalation. XPS characterizations suggest that the carbon fiber sponges are mostly doped with nitrogen in a pyrrolic fashion. Results for C1s and O1s revealed the presence of organic C=O, which could be attributed to carboxylic acids (ethanoic acid) and organic C-O associated to furans, pyrans, epoxies, and ethoxy groups likely attaching themselves at the surface or defected carbon fibers. This result is of particular interest since the presence of these functional groups could explain the super hydrophobicity of the carbon fiber sponges. However, more experimental and theoretical investigations on the origin of the super hydrophobicity in carbon sponges are needed.

References

[1]. A. L. Elias, N. Perea-López, L. Pulickal Rajukumar, A. McCreary, F. López-Urías, H. Terrones, M. Terrones. Chapter 17- Three-dimensional Nanotube Networks and a New Horizon of Applications pp. 457-493 (2014). Elsevier-Book- Nanotube Superfiber Materials 2014. Edited by Mark Schulz,Vesselin Shanov,Zhangzhang Yin.

[2]. Gui, Xuchun; Li, Hongbian; Wang, Kunlin; et al. Recyclable carbon nanotube sponges for oil absorption. *Acta Materiala* 59 (12), 4798-4804, 2011.

[3]. Li, Hongbian; Gui, Xuchun; Zhang, Luhui; et al. Carbon nanotube sponge filters for trapping nanoparticles and dye molecules from water. *Chemical Communications* 46 (42), 7966-7968, 2010.

[4]. Zhong, Jing; Yang, Zhenyu; Mukherjee, Rahul; et al. Carbon nanotube sponges as conductive networks for supercapacitor devices. *Nano Energy* 2 (5), 1025-1030, 2013.

[5]. A.E. Aliev et al. Giant-stroke, super elastic carbon nanotube aerogel muscles. *Science* 323 (5921) (2009) 1575e1578.

[6]. M.A. Correa-Duarte, N. Wagner, J. Rojas-Chapana, C. Morsczeck, M. Thie, M. Giersig, Fabrication and biocompatibility of carbon nanotube-based 3D networks as scaffolds for cell seeding and growth. *Nano Lett.* 4 (11) (2004) 2233e2236.

[7]. X. Gui, J. wei, K. Wang, A. Cao, H. Zhu, Y. Jia, Q. shu, D. Wu. Carbon nanotube sponges. Adv. Mater. 22, 617, 2010.

[8]. C. Shan, W. Zhao, X. L. Lu, D. J. O'Brien, Y. Li, Z. Cao, A. L. Elias, R. Cruz-Silva, M. Terrones, B. Wei, J. Suhr. Three-Dimensional Nitrogen-Doped Multiwall Carbon Nanotube Sponges with Tunable Properties. *Nano Lett.* 13, 5514, 2013.

[9]. M. Crespo, M. González, A. L. Elías, L. P. Rajukumar, J. Baselga, M. Terrones, J. Pozuelo. Ultra-light carbon nanotube sponge as an efficient electromagnetic shielding material in the GHz range. *Phys. Status Solidi RRL* 8, 698, 2014.

[10].A.M. Cassell, G.C. McCool, H.T. Ng, J.E. Koehne, B. Chen, J. Li, J. Han, M. Meyyappan, Carbon nanotube networks by chemical vapor deposition. *Appl. Phys. Lett.* 82 (5) (2003) 817e819.

[11].D.P. Hashim et al. Covalently bonded three-dimensional carbon nanotube solids via boron induced nanojunctions. *Scientific Reports* 2 (2012).

[12]. H. Yu, Z.F. Li, G.H. Luo, F. Wei, Growth of branch carbon nanotubes on carbon nanotubes as support. *Diamond and Related Materials* 15 (9) (2006) 1447e1451.

[13].A.A. El Mel, A. Achour, W. Xu, C.H. Choi, E. Gautron, B. Angleraud, A. Granier, L. Le Brizoual, M.A. Djouadi, P.Y. Tessier, Hierarchical carbon nanostructure design: ultra-long carbon nanofibers decorated with carbon nanotubes. *Nanotechnology* 22 (43) (2011).

[14].X. Sun, R. Li, B. Stansfield, J.P. Dodelet, S. Desilets, 3D carbon nanotube network based on a hierarchical structure grown on carbon paper backing. *Chem. Phys. Lett.* 394 (4e6) (2004) 266e270.

[15].J.A. Rodriguez-Manzo, M.S. Wang, F. Banhart, Y. Bando, D. Golberg, Multibranched junctions of carbon nanotubes via cobalt particles. *Advanced Materials* 21 (44) (2009) 4477.

[16].G.W. Meng, Y.J. Jung, A.Y. Cao, R. Vajtai, P.M. Ajayan, Controlled fabrication of hierarchically branched nanopores, nanotubes, and nanowires. *Proceedings of the National Academy of Sciences of the United States of America* 102 (20) (2005) 7074e7078.

[17].M. Terrones, F. Banhart, N. Grobert, J.C. Charlier, H. Terrones, P.M. Ajayan, Molecular junctions by joining single-walled carbon nanotubes. *Phys. Rev. Lett.* 89 (7) (2002).

[18]. C Singh, MS Shaffer, AH Windle. Production of controlled architectures of aligned carbon nanotubes by an injection chemical vapour deposition method. *Carbon* 41 (2), 359-368, 2003.

[19].Czerw R, Terrones M, Charlier JC, Blase X, Foley B, Kamalakaran R, et al. Identification of electron donor states in N-doped carbon nanotubes. *Nano Lett.* 200; 1(9):457–60.

[20].Terrones M, Romo-Herrera JM, Cruz-Silva E, Lopez-Urıas F, Munoz-Sandoval E, Velazquez-Salazar JJ, et al. Pure and doped boron nitride nanotubes. *Mater Today* 2007;10:30–8.

[21].E. Cruz-Silva et al. Heterodoped Nanotubes: Theory, Synthesis and Characterization of Phosphorus-Nitrogen Doped Multiwalled Carbon Nanotubes. *Acs Nano* 2 (3), 441-448 (2008)

[22].A. Botello-Méndez, J. Campos-Delgado, A. Morelos-Gómez, M. A. Vidal, H. Navarro, H. Terrones, M. Terrones, Controlling the dimensions, reactivity and crystallinity of multiwalled carbon nanotubes using low ethanol concentrations. *Chem. Phys. Lett.* 453 (2008) 55.

[23].Nancy J. Dudney and Jane Y. Howe.Hierarchically Structured Sulfur/Carbon Nanocomposite Material for High-Energy Lithium Battery Chengdu Liang. *Chem. Mater.* 2009, 21 (19), pp 4724–4730.

[24].T. Kato, K. Kusakabe, S. Morooka. Effect of sulfur on formation of vapor-grown carbon-fiber. *J. Mater. Scie. Lett. 13 (5) (1994) 374e377.*

[25].B.C. Satishkumar, P.J. Thomas, A. Govindaraj, C.N.R. Rao. Y-junction carbon nanotubes. *Appl. Phys. Lett.* 77 (16) (2000) 2530e2532.

[26].F.L. Deepak, N.S. John, A. Govindaraj, G.U. Kulkarni, C.N.R. Rao. Nature and electronic properties of Y-junctions in CNTs and N-doped CNTs obtained by the pyrolysis of organometallic precursors. *Chem. Phys. Lett.* 411 (4e6) (2005) 468e473.

[27]. C. Valles, M. Perez-Mendoza, P. Castell, M.T. Martinez, W.K. Maser, A.M. Benito. Towards helical and Y-shaped carbon nanotubes: the role of sulfur in CVD processes. *Nanotechnology* 17 (17) (2006) 4292e4299.

[28]. J.M. Romo-Herrera, B.G. Sumpter, D.A. Cullen, H. Terrones, E. Cruz-Silva, D.J. Smith, V. Meunier, M. Terrones. An atomistic branching mechanism for carbon nanotubes: sulfur as the triggering agent. *Angewandte Chemie, International Edition* 47 (16) (2008) 2948e2953.

[29]. J.M. Romo-Herrera, D.A. Cullen, E. Cruz-Silva, D. Ramirez, B.G. Sumpter, V. Meunier, H. Terrones, D.J. Smith, M. Terrones. The role of sulfur in the synthesis of novel carbon morphologies: from covalent Y-junctions to sea-urchin-like structures. *Advanced Functional Materials* 19 (8) (2009) 1193e1199.

[30].J.A. Rodriguez-Manzo, M.S. Wang, F. Banhart, Y. Bando, D. Golberg. Multibranched junctions of carbon nanotubes via cobalt particles. *Advanced Materials* 21 (44) (2009) 4477.

[31].Wei, J. Q. et al. The effect of sulfur on the number of layers in a carbon nanotube. *Carbon* 2007, 45, 2152−2158.

[32].Laura A. Langley, Daniel E. Villanueva, and D. Howard Fairbrother. Quantification of Surface Oxides on Carbonaceous Materials. *Chem. Mater.* 2006, 18, 169-178.

[33].Mohammad Saleh Shafeeyan, Wan Mohd Ashri Wan Daud, Amirhossein Houshmand, Ahmad Shamiri. A review on surface modification of activated carbon for carbon dioxide adsorption . *Journal of Analytical and Applied Pyrolysis* 89 (2010) 143–151.

[34].V. Datsyuk, M. Kalyva, K. Papagelis, J. Parthenios, D. Tasis, A. Siokou, I. Kallitsis, C. Galiotis. Chemical oxidation of multiwalled carbon nanotubes. *Carbon* 46 (2008) 833–840.

[35].Ge Tao, Zhang Mingxu, Min Fanfei. The XPS analysis of surface texture of different-density-level coking coal of Fenxi county. *International Journal of Oil, Gas and Coal Engineering* 2014; 2(4): 59-65.

[36].Javier Dıaz, Guido Paolicelli, Salvador Ferrer, and Fabio Comin. Separation of the sp^3 and sp^2 components in the C1s photoemission spectra of amorphous carbon films. *Phys. Rev. B* 54 (11), 8064, 1996.

[37]. B. I. Rosario-Castro, E. J. Contes, M. E. Perez-Davis, C. R. Cabrera. Attachment of single-wall carbon nanotubes on platinum surfaces by self-assembling techniques. *Rev. Adv. Mater. Sci.* 10, 381-386 (2005).

[38].D. T. Pham, T. H. Lee, D. H. Luong, F. Yao, A. Ghosh, V. T. Le, et al. Carbon Nanotube-Bridged Graphene 3D Building Blocks for Ultrafast Compact Supercapacitors. ACS Nano 9(2):2018-2027, 2015.

[39].R. Z. Zhang, S. J. He, Y. Z. Lu, W. Chen. Fe, Co, N-functionalized carbon nanotubes in situ grown on 3D porous N-doped carbon foams as a noble metal-free catalyst for oxygen reduction. *J Mater. Chem.* A 3(7):3559-3567, 2015.

[40].R. Du, Q. C. Zhao, N. Zhang. Macroscopic Carbon Nanotube-based 3D Monoliths. *Small* 11(27):3263-3289, 2015.

[41].T. Sharifi, M. Valvo, E. Gracia-Espino, R. Sandstrom, K. Edstrom, T. Wagberg. Hierarchical self-assembled structures based on nitrogen-doped carbon nanotubes as advanced negative electrodes for Li-ion batteries and 3D microbatteries. *J. Power Sources* 279:581-592, 2015.

[42].S. Usmani, E. R. Aurand, M. Medelin, A. Fabbro, D. Scaini, J. Laishram, et al. 3D meshes of carbon nanotubes guide functional reconnection of segregated spinal explants. Sci. Adv. 2: e1600087, 2016.

[43].P, Hohenberg, W. Kohn, Inhomogeneous Electron Gas. *Phys. Rev*. **136**, B864 (1964).

[44].W. Kohn, L.J. Sham, Self-Consistent Equations Including Exchange and Correlation Effects. *Phys. Rev*. 140, A1133 (1965).

[45].J. P. Perdew, A. Ruzsinszky, G. I. Csonka, O. A. Vydrov, G. E. Scuseria, L.A. Constantin, X. Zhou, K. Burke, Restoring the density-gradient expansion for exchange in solids and surfaces. *Phys. Rev. Lett*. 100, 136406 (2008).

[46]. J. M. Soler, E. Artacho, J. D. Gale, A. García, J. Junquera, P. Ordejón, D. Sánchez-Portal, The SIESTA method for ab initio order-N materials simulation. *J. Phys. Condens. Matter* 14, 2745 (2002).

[47]. J. Junquera, O. Paz, D. Sánchez-Portal, E. Artacho, Numerical atomic orbitals for linear-scaling calculations. *Phys. Rev. B* 64, 235111 (2001).

[48].N. Troullier, J. L. Martins, Efficient pseudopotentials for plane-wave calculations. *Phys. Rev. B* 43, 1993 (1991).

[49].L. Kleinman, D. M. Bylander, Efficacious Form for Model Pseudopotentials. *Phys. Rev. Lett.* 48, 1425 (**1982**).

[50].Y. C. Jung, B. Bhusham, Contact angle, adhesion and friction properties of micro- and nanopatterned polymers for superhydrophobicity. *Nanotechnology* 17(19):4970-4980, 2006.

[peng] L. Peng, S. Yuan, G. Yan, P. Yu, Y. B. Luo, hydrophobic sponge for spilled oil absorption. J. Appl. Polym. Sci. 131(20):40886, 2014.

[yuan] J. K. Yuan, J. Yuan, X. G. Liu, O. Akbulut, J. Q. Hu, S. L. Suib, et al. Superwetting nanowire membranes for selective absorption, Nat. Nanotecnol. 3(6): 332-336, 2008.

[lau] K. K. S. Lau, J. Bico, K. B. K. Teo, M. Chhowalla, G. A. J. Amaratunga, W. I. Milne, G. H. McKinley, K. K. Gleason, Superhydrophobic Carbon Nanotube Forests, Nano Lett. 3(12):1701-1705, 2003.

We have also added the following references:

38 P, Hohenberg, W. Kohn, Inhomogeneous Electron Gas. *Phys. Rev*. 136, B864 (1964).

39 W. Kohn, L.J. Sham, Self-Consistent Equations Including Exchange and Correlation Effects. *Phys. Rev*. 140, A1133 (1965).

40 J. P. Perdew, A. Ruzsinszky, G. I. Csonka, O. A. Vydrov, G. E. Scuseria, L.A. Constantin, X. Zhou, K. Burke, **Restoring the density-gradient expansion for exchange in solids and surfaces.** *Phys. Rev. Lett*. **100, 136406 (2008).**

41 J. M. Soler, E. Artacho, J. D. Gale, A. García, J. Junquera, P. Ordejón, D. Sánchez-Portal, **The SIESTA method for ab initio order-N materials simulation.** *J. Phys. Condens. Matter* **14, 2745 (2002).**

42 J. Junquera, O. Paz, D. Sánchez-Portal, E. Artacho, **Numerical atomic orbitals for linear-scaling calculations.** *Phys. Rev. B* **64, 235111 (2001).**

43 N. Troullier, J. L. Martins, **Efficient pseudopotentials for plane-wave calculations.** *Phys. Rev. B* **43, 1993 (1991).**

44 L. Kleinman, D. M. Bylander, **Efficacious Form for Model Pseudopotentials.** *Phys. Rev. Lett.* **48, 1425 (1982).**

Tables and Captions

Table 1: Emilio Muñoz-Sandoval et al.

Sample	Gravity center	$d_{002(\gamma)}$, $d_{002(\pi)}$	Intensity	FWHM	Integrated area (%)
S1	23.62	3.762	141.83	4.30	38.34
	25.92	3.433	392.32	2.80	61.65
S2	23.82	3.731	76.07	5.59	43.93
	25.82	3.446	216.52	2.58	56.06
S3	24.82	3.582	29.47	5.58	75.17
	26.03	3.419	30.64	1.76	24.82
S4	25.40	3.502	130.61	1.99	80.80

	26.29	3.385	73.63	1.08	19.19
S5	25.66	3.467	292.15	1.86	75.62
	26.47	3.363	260.09	0.84	24.37
S6	25.45	3.495	35.93	4.99	71.78
	26.34	3.379	107.69	0.68	28.21

Table 1: Data of the deconvolution C(002) peak in two bands:γ-band (red color) and the π band (black color) for the different samples labeled by S1, S2, S3, S4, S5, and S6. The angle (2θ) peak position (gravity center), the interlayer spacing (d_{002}), the peak intensity, the full width at half maximum (FWHM) and the area under the curves. The integrated area of the π-band is related to the number of aromatic atoms or graphitization whereas the integrated area of γ band indicates the quantity of disorder in the graphitic structures.

Table 2: Emilio Muñoz-Sandoval et al.

Sample	Bond	Gravity center (eV)	FWHM	Integrated area %
S1	sp^2-carbon	284.27	1.30	74.7
	sp^3-carbon	285.51	1.30	25.3
S2	Fe-C	282.86	0.71	4.5
	sp^2-carbon	284.19	1.57	85.6
	C=O	285.91	1.00	9.8
S3	sp^2-carbon	284.26	1.09	70.6
	sp^3-carbon	285.17	2.02	29.4

S4	sp^2-carbon	284.62	1.44	57.4
	sp^3-carbon	285.07	1.42	33.6
	C=O	286.38	1.10	57.4
S5	sp^2-carbon	284.66	1.21	80.8
	sp^3-carbon	285.98	0.18	17.4
	C=O	287.12	0.56	1.8
S6	sp^2-carbon	284.35	1.04	16.4
	sp^3-carbon	285.34	1.42	49.6
	C=O	286.05	2.03	34.0

Table 2: Data of the deconvolution C1s spectrum for samples S1-S6. The sp^3 signal could be correlated with the presence of ethoxy groups anchored on the carbon materials (CH$_3$CH$_2$O-) whereas organic C=O suggest the presence of carboxylic acids (CH$_3$COOH). The peak at 286 eV can be also attributed to Cα carbons and 285.5 eV can be associated with C-O and C-N bonds.

Table 3: Emilio Muñoz-Sandoval et al.

Sample	Bond	Gravity center (eV)	FWHM	Integrated area %
S1	Quaternary-N	400.48	2.75	46.2
	Pyrrolic-N	399.67	1.67	42.2
	Pyridinic-N	398.18	1.00	11.6
S2	Pyrrolic-N	399.22	1.52	54.5
	Pyridinic-N	398.28	1.30	45.5
S3	Quaternary-N	401.55	1.29	32.2
	Pyrrolic-N	400.39	1.04	26.0
	Pyridinic-N	399.12	1.68	41.8
S4	Quaternary-N	400.79	1.80	29.3
	Pyrrolic-N	399.85	1.49	53.1
	Pyridinic-N	398.91	1.17	17.5
S5	Quaternary-N	401.41	1.95	52.5
	Pyrrolic-N	400.52	1.37	25.0
	Pyridinic-N	398.76	1.38	22.5
S6	Quaternary-N	401.11	1.89	50.1
	Pyrrolic-N	400.08	1.14	31.5
	Pyridinic-N	399.14	1.12	18.4

Table 3: Data of the deconvolution N1s spectrum for samples S1-S6. The binding energies for the N-doping types are: **401.2-402.2** eV (quaternary-N), **399.8-401.2** eV (pyrrolic-N), and **398.1-399.8** eV (pyridinic-N).

Table 4: Emilio Muñoz-Sandoval et al.

Sample	bond	Gravity center (eV)	FWHM	Integrated area %
S1	Fe(OH)O	530.38	1.12	4.6
	C-O	532.05	1.55	59.2
	C=O	533.33	1.53	36.2
S2	Fe(OH)O	531.01	1.46	10.9
	C-O	531.95	1.26	82.9
	C=O	533.09	0.83	6.2
S3	Fe(OH)O	530.39	1.59	7.5
	C-O	531.94	1.68	60.5
	C=O	533.27	1.94	31.9
S4	C-O	531.55	1.33	60.8
	C=O	532.48	1.22	38.5
	COOH	533.60	1.54	37.9
S5	C-O	532.38	1.77	39.2
	C=O	532.93	1.47	37.7
	COOH	534.14	1.27	23.1
S6	C-O	532.53	1.61	50.4
	C=O	533.75	1.37	38.8
	COOH	534.86	1.06	10.7

Table 4: Data of the deconvolution O1s spectrum for samples S1-S6. The organic C-O bonds could be due to an ethoxy molecule (ethanol without the H atoms, that attached to the oxygen) whereas C=O bonds signal suggests the presence of carboxylic acids (CH_3COOH). The small traces of C-O-C or C-OH (~234 eV) functional groups could be attributed to pyrone, chromene, lactone, and lactol.

Figures and Captions

Figure 1: Emilio Muñoz-Sandoval et al.
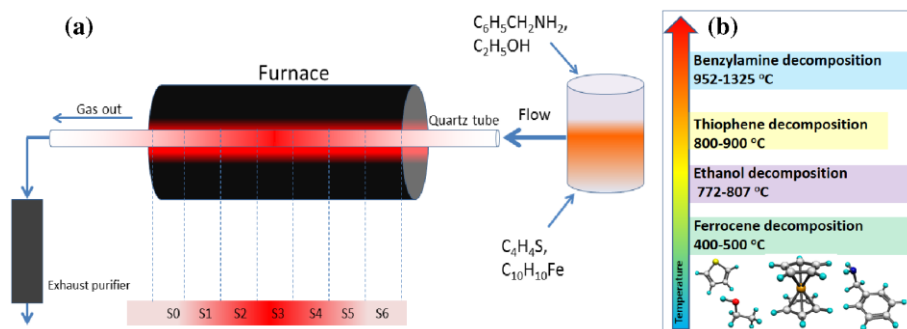
Figure 1: (a) Schematic representation of the chemical vapor deposition setup used to synthesize the carbon sponges. A solution containing ethanol, benzylamine, thiophene and ferrocene was pyrolyzed at 1020 °C under an argon-hydrogen flow. The resulting material was collected from the reaction quartz tube by scraping its inner walls. The samples were classified according to the region in the tubular furnace labeled by S1, S2, S3, S4, S5, and S6. **(b)** Decomposition temperature of the used precursors and ball-and-stick models of thiophene (C_4H_4S), ethanol (CH_3CH_2OH), ferrocene ($Fe(C_5H_5)_2$), and benzylamine ($C_6H_5CH_2NH_2$) molecules (yellow: sulfur, red: oxygen, gray: carbon, cyan: hydrogen, blue: nitrogen, and orange: iron).
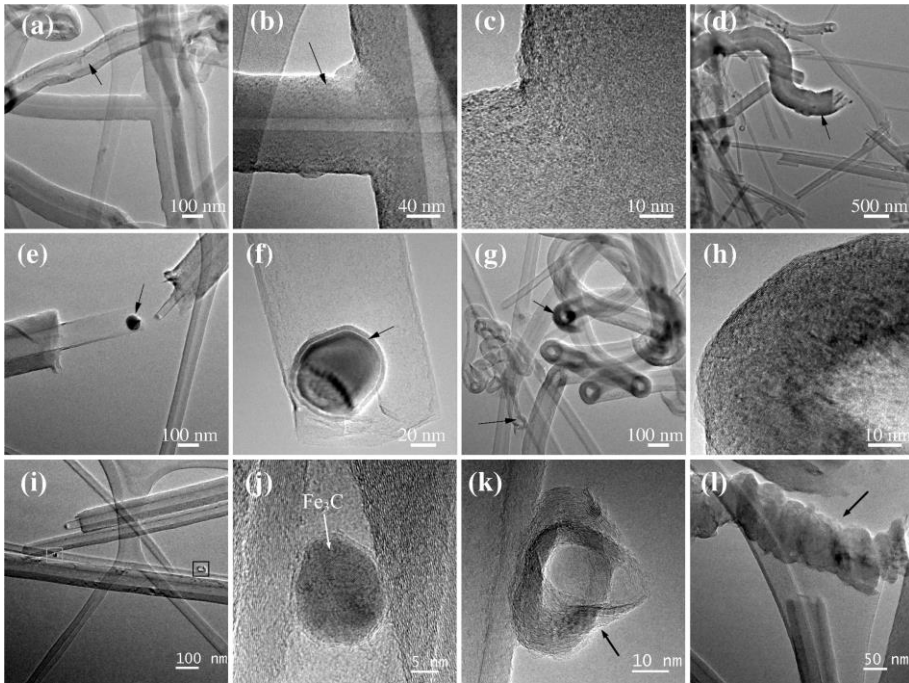
Figure 2: Emilio Muñoz-Sandoval et al.
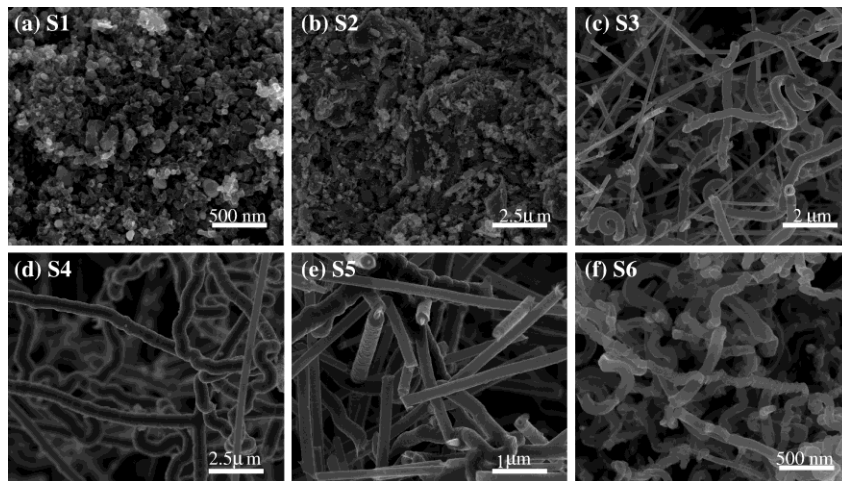
Figure 2: Scanning electron microscopy (SEM) images of samples produced at 1020 °C with an Ar-H$_2$ flow of 0.8 l/min. The images correspond to samples collected at S1, S2, S3, S4, S5, and S6 zones (see figure 1). Notice that five types of materials are involved along the furnace. In samples S1 and S2 (in the furnace exit) flakes formed by multilayered graphite-like materials are obtained. Sample S3 exhibits the presence of wavy and straight carbon fibers. Sample S4 presents preferentially wavy carbon fibers. Sample S5 has mostly straight carbon fibers. In sample S6, carbon ripped graphite ribbons and tubular shells are formed by graphite materials, in other S6 images (do not show here) very few straight carbon fibers similar to that obtained in S5 were observed.

Figure 3: Emilio Muñoz-Sandoval et al.
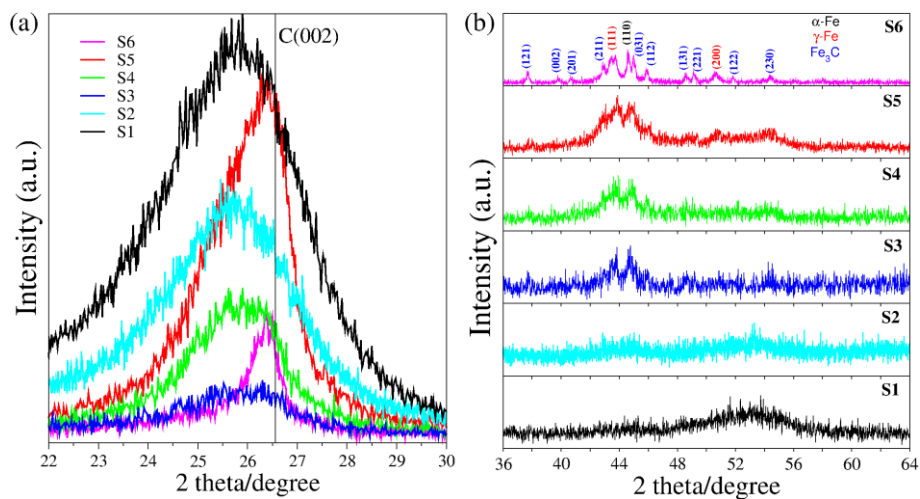
Figure 3: XRD patterns of samples S1, S2, S3, S4, S5, and S6 fabricated at 1020 °C and 0.8 l/min Ar-H_2 flow. **(a)** The C(002) peak is attributed to the graphitic materials. **(b)** Angle range where the trace of the catalytic particles are observed, the associated signals for bulk-Fe_3C and bulk-γ-Fe are indexed. Results on the deconvoluted peak in **(a)** can be seen in table 1. Notice that a downshift in the center of gravity of the (002) can be appreciated, which could indicate the presence of other types of carbon material; possibly turbostratic graphitic or foreign atoms hosted within the graphitic layers.

Figure 4: Transmission electron microscopy (SEM) images of samples produced at 1020 °C with an Ar-H_2 flow of 0.8 l/min. All the images correspond to samples collected at **S6 zone**. **(a)** carbon fibers composed by multiwalled carbon nanotubes covered by thick amorphous carbon material (see the black arrow), **(b)** and **(c)** high magnification of the carbon fiber, **(d)** wavy carbon fiber containing a well-graphite few layered carbon nanotube, **(e)** carbon fiber containing a iron-base nanoparticle at the tip, **(f)** wavy carbon fibers, **(g)** wavy carbon fiber , **(h)** tip of wavy fibers, **(i)** straight carbon fibers, the enclosed area by the squares are displayed in **(j)** and **(k)** showing a Fe-base nanoparticle, very probably as Fe3C considering the X-ray results, and a single walled carbon nanotube, and **(l)** ripped graphite ribbons.
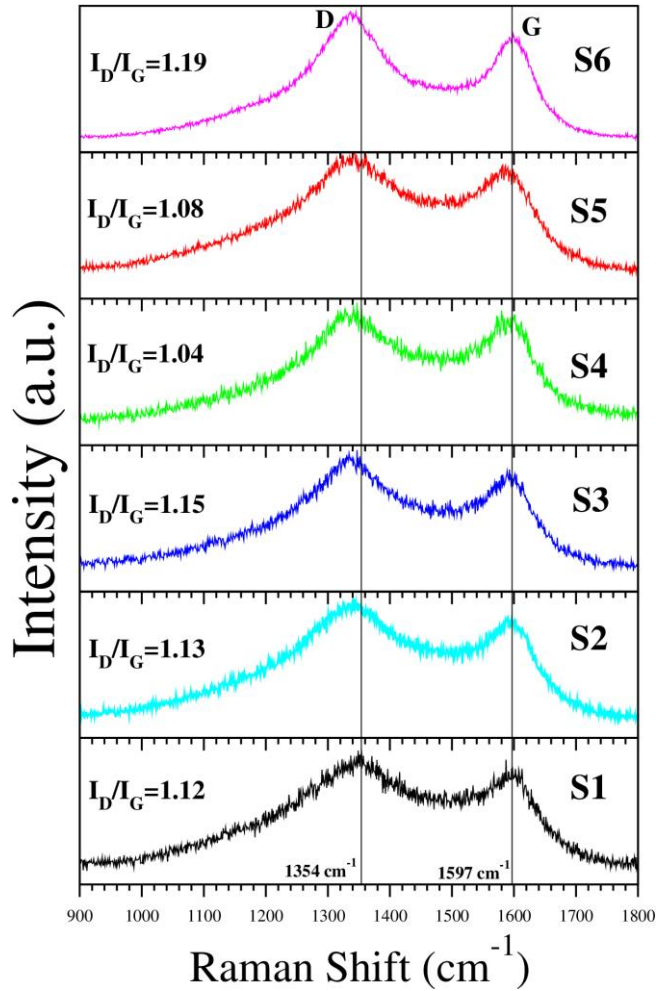
Figure 5: Raman spectra from different synthesized samples using an excitation source of 633 nm (1.958 eV) laser. The D- and G-bands 1354 cm[1] and 1597 cm[1], respectively for graphite are indicated by the vertical line. The values of the intensity ratios of I_D/I_G are also shown; large values of I_D/I_G indicate the existence of disordered carbon material.
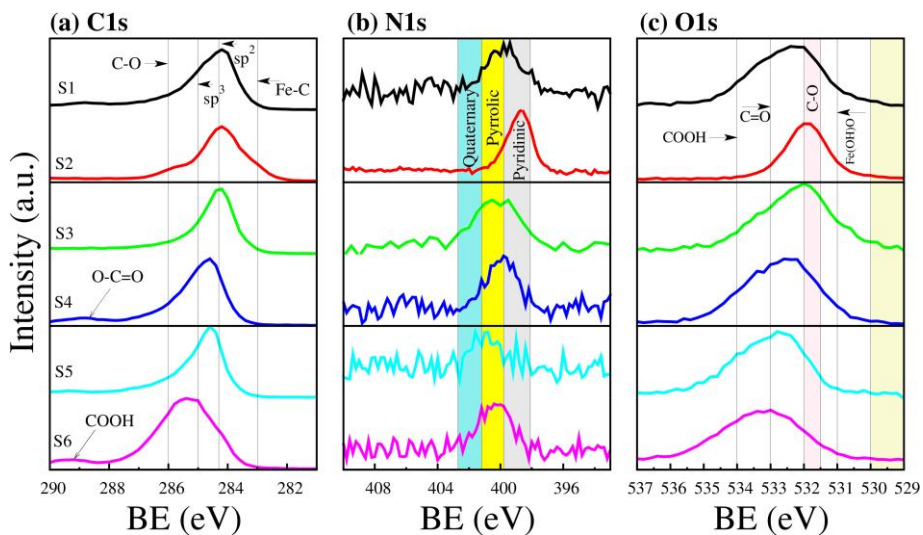
Figure 6: X-ray photoelectron spectroscopy (XPS) analysis performed on samples. **(a)** C 1s line scan shows a sp^2-hybridized C signal and a broad shoulder containing a signal coming from oxygenated carbon groups and C−N. **(b)** N 1s line scan exhibits a broad N signal, which can be composed by quaternary N **(401.2-402.2 eV)**, pyrrolic N **(399.8-401.2 eV)**, and pyridinic N **(398.1-399.8 eV)**. **(c)** O 1s line scan exhibits the presence of oxygen. Results of C1s, N1, O1s deconvoluted peaks are shown in table 2, 3, and 4 respectively. Notice that the peaks at 288 and 288.5 eV in C1s can be also attributed to C-C(O)-NR and C-C(O)-OR functional groups.
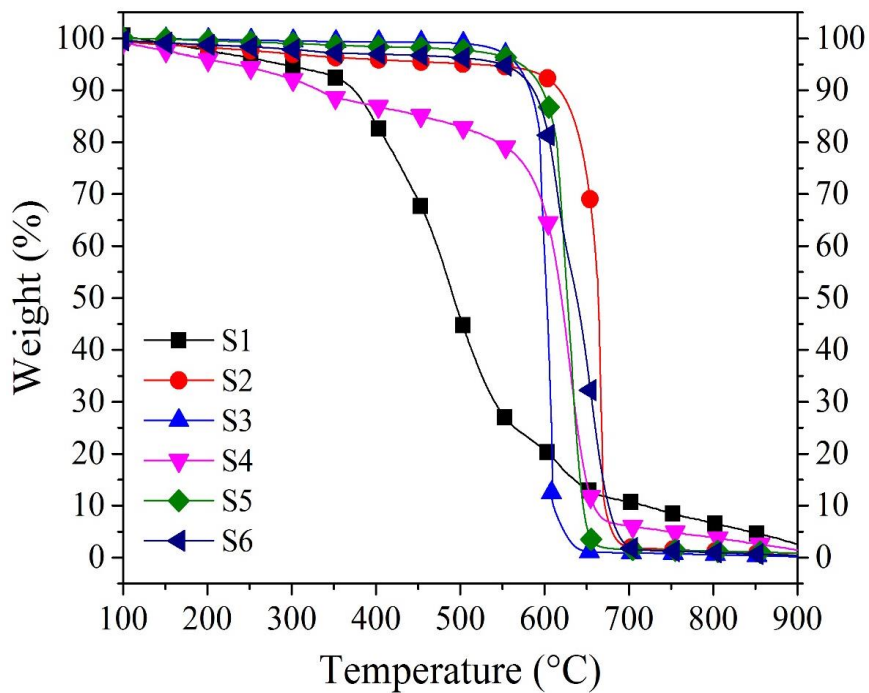
Figure 7: Thermogravimetric analysis (TGA) of carbon nanotube sponges for samples S1-S6. Note that the oxidative temperatures are similar to that found in carbon nanotubes. The progressive weight loss at 100-600 °C for the samples S4 and S1 could be an indication of defected graphitic layers as we have confirmed by other techniques of characterization.

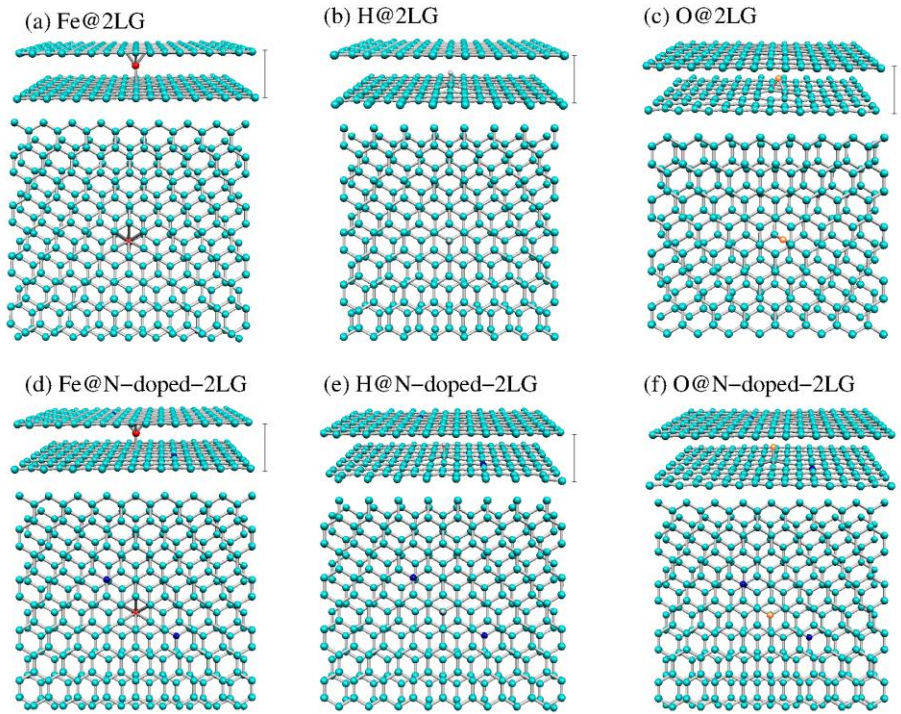**Figure 8:** Emilio Muñoz-Sandoval et al.

Figure 8: Relaxed two layers graphene (2LG) containing Fe, H, or O inside: **(a)** Fe@2LG, **(b)** H@2LG, and **(c)** O@2LG. For **(d)**, **(e)**, and **(f)** the graphene layers were doped with nitrogen. The interlayer space variation was of **3.54**, **3.75**, and **4.89** Å for Fe@2LG, H@2LG, and O@2LG, respectively. For N-doped graphene, the interlayer distance was of **3.58**, **3.75**, and **4.42** Å for Fe@N-doped-2LG, H@N-doped-2LG, and O@N-doped-2LG, respectively.

Figure 9: Emilio Muñoz-Sandoval et al.
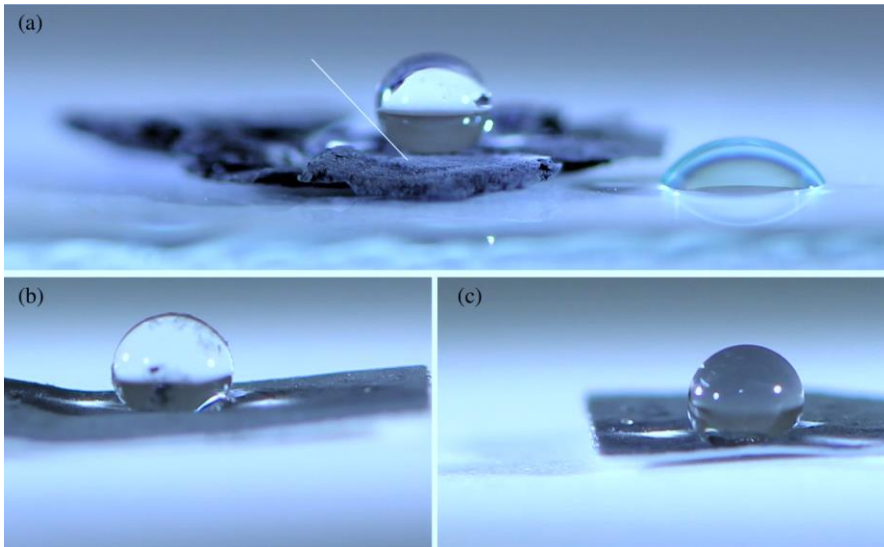
Figure 9: Optical images of water droplets (2.86 mm diameter) showing the super hydrophobic surface of carbon sponge type nanostructures (CSTN) collected from S4 zone. In this case the estimated contact angle was around 145° (see Table SI-3). **(b)** and **(c)** images depict foils made of CSTN. The foils were fabricated in the following way: CSTN were sonicated in an ethanol solution during 2 h and filtered on a nylon membrane under vacuum filtration. Note that the super-hydrophobic property persists.

Figure 10: Emilio Muñoz-Sandoval et al.
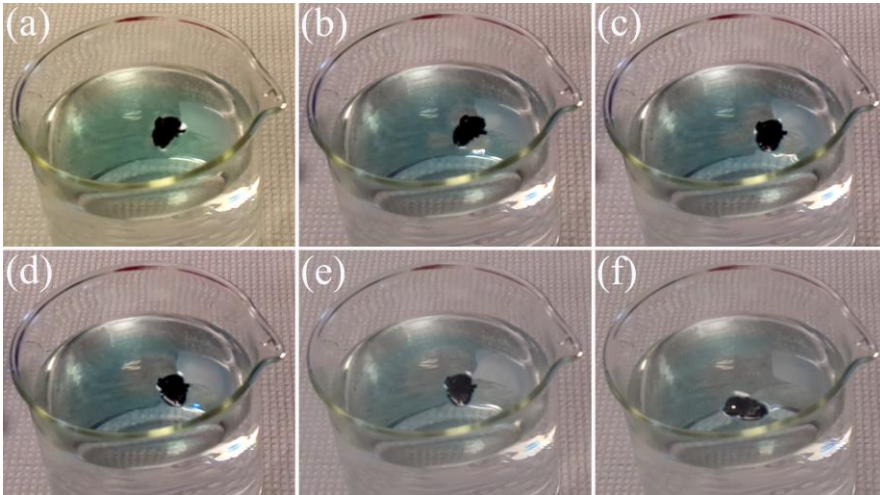
Figure 10: Oil Absorption test of sponge-type structures: **(a)** 0 s, **(b)** 3 s, **(c)** 6 s, **(d)** 13 s, **(e)** 31 s, and **(f)** 57 s. Note that the formation of transparent zones around the CSTN. Cooking oil (canola oil) was used which was colored with oil color. The absorption is conducted quickly at the start of the process and subsequently becomes slower due to the oil-absorption saturation.
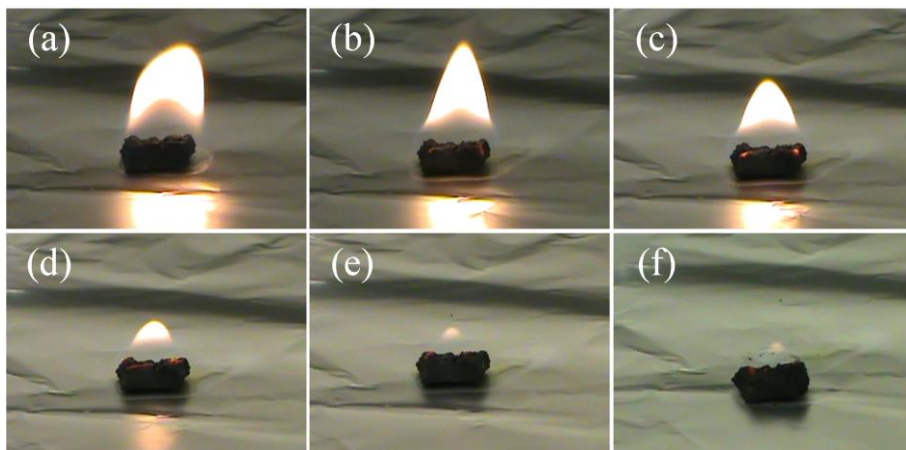
Figure 11: Emilio Muñoz-Sandoval et al.

Figure 11: Burning process of CSTN sample for different times. **(a)** 1 minute 25 seconds, **(b)** 1 minute 35 seconds, **(c)** 1 minute 47 seconds, **(d)** 2 minutes 10 seconds, **(e)** 2 minutes 31 seconds and **(f)** 2 minutes and 45 seconds. The total time to burn all the oil was 3 minutes and 7 seconds.

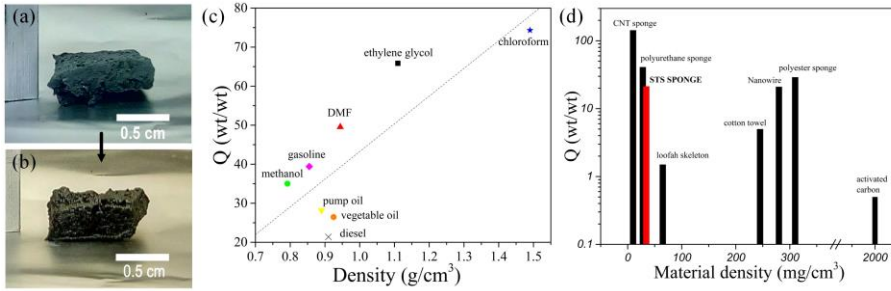**Figure 12:** Emilio Muñoz-Sandoval et al.

Figure 12: **(a)** Photo of CSTN with a volume of 0.149 cm^3 before the absorption experiment. **(b)** CSTN after absorbing vegetable oil. It absorbs 26 times its weight. **(c)** Absorption capacity for different oil/solvent measured from CSTN. The capacity absorption increases for high oil/solvent densities, reaching 74 times its weight for chloroform. **(d)** Absorption capacity of several materials reported in Ref. 7 and compared with our CSTN material (red bar).
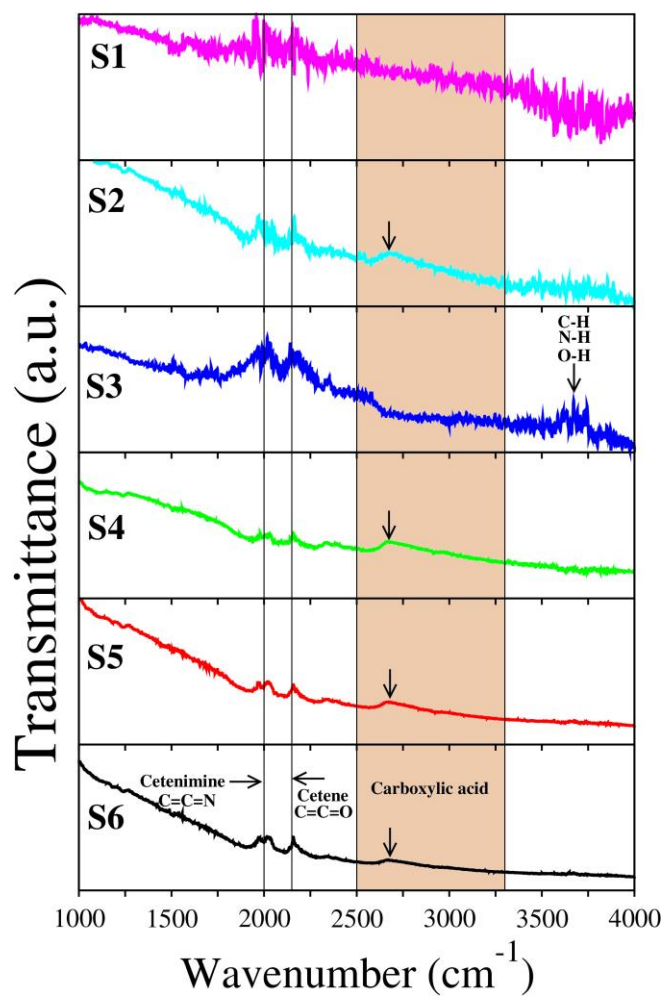
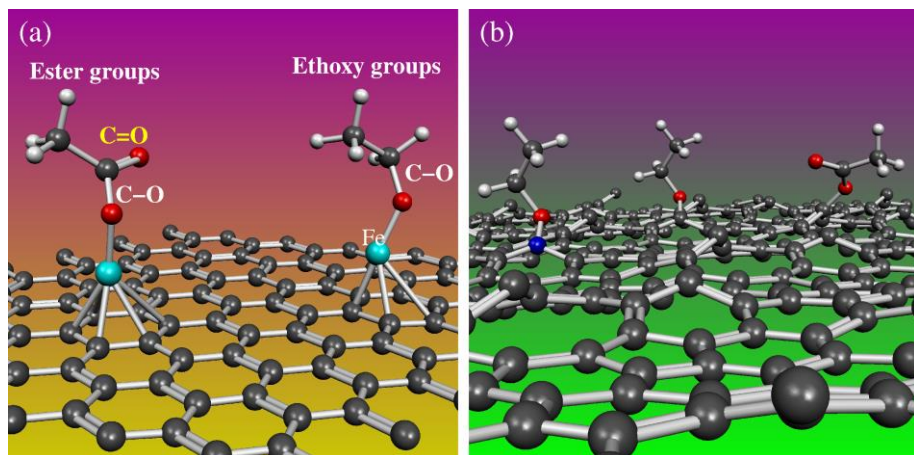**Figure 13:** Fourier transform infrared (FTIR) spectra of CSTN for samples S1-S6.

Figure 14. Two probable anchorage scenarios of ester and ethoxy groups to the surface of the CSTN: (a) Ethoxy and ester groups are anchored to CSTN surface via Fe atom; (b) These hydrophobic group are also attached to the CSTN surface via nitrogen functionalities or vacancies.